An in-depth investigation of AFm-NO3 hydrates: Fe to Al substitution, hydration levels and anionic exchange capabilities

Aurore Lechevallier, Mohend Chaouche, Jérôme Soudier, Evelyne Prat, Guillaume Renaudin

Cement and Concrete Research 186 (2024) 107680

Contents lists available at ScienceDirect

Cement and Concrete Research

journal homepage: www.elsevier.com/locate/cemconres

An in-depth investigation of AFm-NO_3 hydrates: Fe to Al substitution, hydration levels and anionic exchange capabilities

Aurore Lechevallier [a,b,c], Mohend Chaouche [c], Jérôme Soudier [b], Evelyne Prat [b], Guillaume Renaudin [a,*]

[a] Université Clermont Auvergne, Clermont Auvergne INP, CNRS, ICCF, F-63000 Clermont-Ferrand, France
[b] Sika, Le Bourget, France
[c] Université Paris-Saclay, CNRS, LMPS, Gif-sur-Yvette, France

ARTICLE INFO

Keywords:
AFm-NO_3 phase
Low-CO_2 binder
Layered double hydroxides
Solid solution

ABSTRACT

The study of mixed Al^{3+}/Fe^{3+} nitrate hydrates is gaining increasing interest with the emergence of new hydraulic binders and Supplementary Cementitious Materials (SCMs) containing significant amounts of iron and aluminum oxides that can be activated by nitrate addition. Layered AFm-NO_3 hydrates containing varying proportions of trivalent Al^{3+} and Fe^{3+} cations were synthesized and characterized. The AFm-NO_3 phase constitutes a continuous solid solution between the two end-members $Ca_2Al(OH)_6{\cdot}NO_3{\cdot}2H_2O$ and $Ca_2Fe(OH)_6{\cdot}NO_3{\cdot}2H_2O$. The obtained $Ca_2Al_{1-x}Fe_x(OH)_6{\cdot}NO_3{\cdot}yH_2O$ solid solution proves stable for four hydration states, with a significant impact on the interlayer distance: $y = 5$ (at high relative humidity with an interlayer distance of 10.4 Å), $y = 2$ (at ambient conditions with an interlayer distance of 8.6 Å), $y = 1$ (above 60 °C with an interlayer distance of 7.4 Å) and $y = 0$ (anhydrous above 175 °C with an interlayer distance of 8.0 Å). In fact, thermal variations reveal some differences between the two Al-rich and Fe-rich sides. Finally, AFm-NO_3 stability was examined in the presence of other anions, demonstrating the low stability of NO_3^- with respect to Cl^- and CO_3^{2-} anions.

1. Introduction

The increase in anthropogenic CO_2 emissions and their impact on the greenhouse effect has led to increased social awareness and a shift in business and economic paradigms. As a result, the CO_2 footprint has become a decisive factor in product selection. This concern is particularly relevant to Ordinary Portland Cement (OPC), given that the cement industry contributes to approximately 8 % of global CO_2 emissions [1].

In response to this context, various new types of hydraulic binders with better environmental credentials have been investigated and proposed as potential substitutes for OPC. Many of these alternatives are composed, in part, of iron and aluminum oxides and typically feature the $Ca_4Al_{2-x}Fe_{2+x}O_{10}$ mixed oxide (i.e. $C_4A_{2-x}F_x$ – with $0.67 \leq x \leq 2$ – in cementitious notation; noted C_4AF in the following), known by the mineralogical name of brownmillerite [2,3]. Calcium-based layered hydrates (i.e. AFm phases) can be formed during the hydration process of brownmillerite [4]. The AFm phases are part of a broader group of 2D compounds known as layered double hydroxides (LDH) of general formula $[M^{II}_{1-x}M^{III}_x(OH)_2]^{x+}{\cdot}(A^{n-}_{x/n}){\cdot}yH_2O$. Their structure consists of a positively-charged main layer $[M^{II}_{1-x}M^{III}_x(OH)_2]^{x+}$ with both M^{II} and M^{III} cations distributed on a single crystallographic site (octahedrally coordinated by hydroxyl groups) and anionic species A^{n-} located in the center of the interlayer with the water molecules. In the case of the AFm sub-family, the divalent cation Ca^{2+} has a larger ionic radius ($R^{2+}_{Ca} = 1.00$ Å) compared to the trivalent cations ($R^{3+}_{Al} = 0.535$ Å, $R^{3+}_{Fe} = 0.645$ Å) at the origin of their crystallographic ordering, which leads to the main layer composition of $[Ca_2M^{III}(OH)_6]^+$ ($M^{III} = Al^{3+}$ or Fe^{3+}) with a fixed Ca/M^{III} atomic ratio of 2. The larger ionic radius of Ca^{2+} cations also requires an increase in its coordination with 6 neighboring hydroxyls, to which is added either an apical water molecule or an anion from the interlayer (Ca^{2+} is then seven-fold coordinated). This has the effect of structuring the interlayer region by a defined hydrogen bond network, as well as providing the precise location of the charge-compensating anion. Fig. 1 shows the general crystal structure representations of LDH of the hydrotalcite type, [5] and AFm of the hydrocalumite type, [6]; illustrating the structural difference brought by the seven-fold coordination of Ca^{2+}. The anions generally encountered in cement chemistry are CO_3^{2-}, SO_4^{2-}, Cl^-, and NO_3^-. The present work

* Corresponding author.
E-mail address: guillaume.renaudin@sigma-clermont.fr (G. Renaudin).

https://doi.org/10.1016/j.cemconres.2024.107680
Received 26 March 2024; Received in revised form 29 August 2024; Accepted 12 September 2024
Available online 18 September 2024

focuses on the AFm-NO_3 phases. $Ca(NO_3)_2$, known as a common accelerator of C_4AF phase hydration [7], favors the rapid formation of this AFm-NO_3 phase, with $[Ca_2Al_{1-x}Fe_x(OH)_6]^+\cdot[NO_3^-\cdot 2H_2O]$ as the expected composition. The Al-pure AFm-NO_3 crystal structure has been described in detail thanks to X-ray single crystal diffraction [8]: a trigonal $P\bar{3}c1$ space group (a = 5.7445 Å and c = 17.235 Å; Table 1) with nitrate anions perpendicular to the main layer and bonded to Ca^{2+}, leading to a large interlayer distance of 8.62 Å (Fig. 1b). This trigonal description has since been used in the literature on powder samples of the same $[Ca_2Al(OH)_6]^+\cdot[NO_3^-\cdot 2H_2O]$ composition [9]. On the other hand, studies performed on the Fe-pure AFm-NO_3 analog have never used this $P\bar{3}c1$ trigonal space group, despite similar (00l) diffraction peak positions [10,11]. Al to Fe solid solutions may occur for AFm phases due to the close ionic radii for trivalent Al^{3+} (R^{3+}_{Al} = 0.535 Å) and Fe^{3+} (R^{3+}_{Fe} = 0.645 Å); this is reflected in cementitious shorthand, AFm meaning Aluminate-Ferrite-monosubstituent hydrate phase [9]. To the best of the authors' knowledge, no study has yet been carried out on the existence, or the extent, of such a $[Ca_2Al_{1-x}Fe_x(OH)_6]^+\cdot[NO_3^-\cdot 2H_2O]$ solid solution.

Investigating the whole $[Ca_2Al_{1-x}Fe_x(OH)_6]^+\cdot[NO_3^-\cdot 2H_2O]$ series is thus a prerequisite to properly characterizing the hydration products of the above-mentioned new low-CO_2 binders, and to understand their hydration mechanism from early age to the long term. The AFm phases naturally form during the hydration of hydraulic binders containing iron and/or aluminum oxides. As cementitious materials are in permanent interaction with the ambient environment, which changes over the seasons (humidity and temperature), it is important to characterize the existence of different hydration levels and also to investigate the potential exchanges with other anionic species in contact (Cl^-, CO_3^{2-}). Beyond their role in low-carbon alternative cement, AFm-NO_3 phases could be significant for durability and multifunctionality studies, such as corrosion inhibition through potential anion exchange from NO_3^- to Cl^-. Additionally, their application in air purification, combined with photocatalytic cementitious materials, offers a promising approach for NO_x sequestration and enhanced environmental protection. Table 1 presents the different hydration levels determined in the literature for the aluminate $Ca_2Al(OH)_6\cdot NO_3\cdot yH_2O$ hydrates, with y varying from 1 to 5, with an interlayer distance varying respectively from 8.0 to 10.5 Å. It appears that the hydrate in equilibrium with a wet paste is $Ca_2Al(OH)_6\cdot NO_3\cdot 5H_2O$, whereas the hydrate which is stable in ambient conditions is $Ca_2Al(OH)_6\cdot NO_3\cdot 2H_2O$. Although there are fewer studies on the Fe-based AFm-NO_3 phase, very similar information was obtained (Table 1).

Table 1
Hydration levels of the AFm-NO_3 phases encountered in the literature.

Hydration level	d_{00l}	Space group, lattice parameters	Ref.
Al-based AFm-NO_3			
$Ca_2Al(OH)_6\cdot NO_3\cdot 1.5H_2O$	8.6 Å		[12]
$Ca_2Al(OH)_6\cdot NO_3\cdot 1.5H_2O$	8.66 Å		[13]
$Ca_2Al(OH)_6\cdot NO_3\cdot\sim 2H_2O$	8.62 Å	a = 5.74 Å, c = 17.24 Å	[14]
No information	From 8.0 to 10.5 Å		[15]
$Ca_2Al(OH)_6\cdot NO_3\cdot 5H_2O$ (wet)	10.43 Å		[16]
$Ca_2Al(OH)_6\cdot NO_3\cdot 3H_2O$	8.86 Å		
$Ca_2Al(OH)_6\cdot NO_3\cdot\sim 2.5H_2O$	8.78 Å		
$Ca_2Al(OH)_6\cdot NO_3\cdot 2H_2O$ (RT)	8.617 Å	$P\bar{3}c1$, a = 5.7445 Å, c = 17.235 Å	[8]
$Ca_2Al(OH)_6\cdot NO_3\cdot 1H_2O$ (70 °C)	8.053 Å	$R\bar{3}c$, a = 5.731 Å, c = 48.32 Å	[17]
Wet	10.49 Å		[9]
35 % RH, 72 h	8.77 Å		
35 % RH, 3 months	8.64 Å		
Dried at 85 °C	8.60 Å		
Dried at 85 °C, then 1 day 25 °C	8.64 Å		
Fe-based AFm-NO_3			
$Ca_2Fe(OH)_6\cdot NO_3\cdot 1.75H_2O$	8.70 Å	a = 5.88 Å, c = 8.70 Å	[18]
$Ca_2Fe(OH)_6\cdot NO_3\cdot nH_2O$ (n > 2)	10.33 Å	a = 5.89 Å, c = 10.33 Å	
100 % RH	10.32 Å	a = 5.887 Å, c = 10.321 Å	[19,20]
$Ca_2Fe(OH)_6\cdot NO_3\cdot 2H_2O$ (35 % RH)	8.64 Å	a = 5.888 Å, c = 8.636 Å	
β-$Ca_2Fe(OH)_6\cdot NO_3$ (85 °C)	8.00 Å		
α-$Ca_2Fe(OH)_6\cdot NO_3$ (85 °C)	7.33 Å		

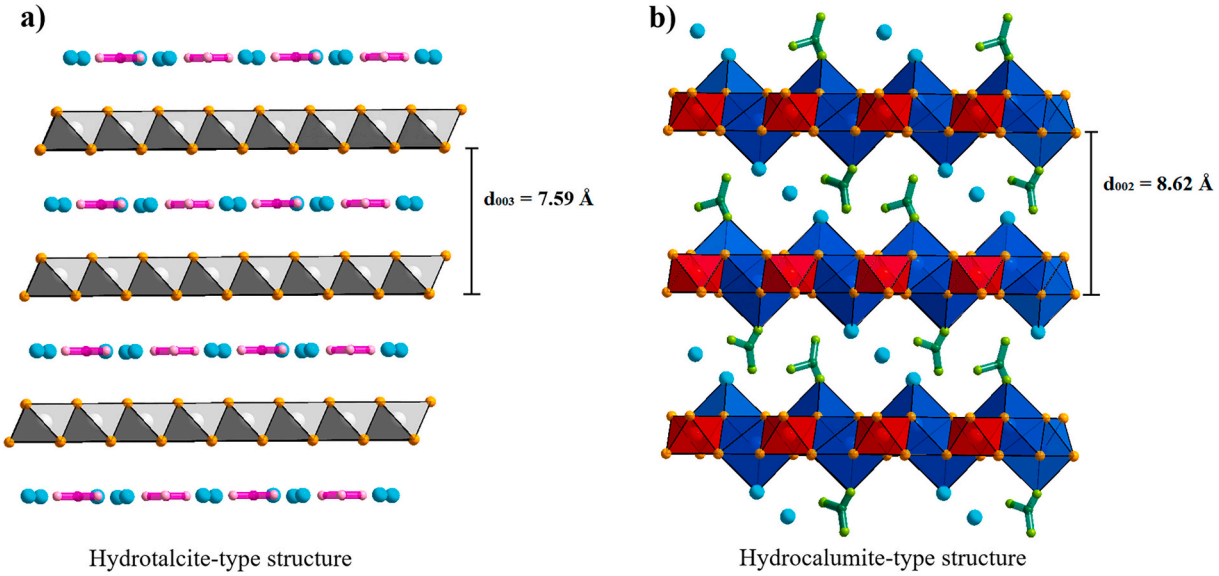

Fig. 1. Cristal structure representations of layered materials: a) $Mg_2Al(OH)_6\cdot(CO_3)_{0.5}\cdot 3H_2O$ LDH compound with hydrotalcite-type structure (divalent Mg^{2+} and trivalent Al^{3+} statistically distributed in the same grey octahedra, pink carbonate anions together with blue water molecules in the interlayer center) and b) $Ca_2Al(OH)_6\cdot(NO_3)\cdot 2H_2O$ AFm compound with hydrocalumite-type structure (sevenfold coordinated divalent Ca^{2+} in the blue polyhedra, trivalent Al^{3+} ordered in the red octahedra, Ca^{2+} bonded to green nitrate anions as well as to half of the blue water molecules, and half the blue water molecules in the interlayer center). (For interpretation of the references to color in this figure legend, the reader is referred to the web version of this article.)

2. Materials and methods

2.1. Synthesis of AFm phases

A series of AFm phases of composition $Ca_2Al_{1-x}Fe_x(OH)_6{\cdot}NO_3{\cdot}2H_2O$ with $x = 0.00$, 0.17, 0.33, 0.50, 0.67, 0.83, and 1.00, were synthesized using the coprecipitation method at room temperature [21]. Syntheses were carried out at the same constant pH. To do this, $Ca(NO_3)_2{\cdot}4H_2O$, $Al(NO_3)_3{\cdot}9H_2O$, and/or $Fe(NO_3)_3{\cdot}9H_2O$ were dissolved in distilled water, maintaining a Ca/(Al + Fe) molar ratio of 2. The amount of dissolved salts was adjusted to obtain the targeted trivalent stoichiometry. Subsequently, 25 mL of a 0.3 M salt solution was added to a reactor containing 100 mL of a 0.2 M NaOH solution under vigorous stirring. Throughout the synthesis process, precautions were taken to prevent carbonate contamination from the air by conducting the procedure under a nitrogen gas flow. The pH was strictly regulated at 13.5 by carefully adding a 2 M NaOH solution by computer control. The suspension was then aged for 24 h in the reactor. The resulting slurry was subjected to centrifugation and underwent three washes with ethanol to eliminate any sodium or nitrate salt residue, and to evacuate liquid water. It should be noted that this step could not be performed under nitrogen; carbonation of the sample may thus potentially occur. Finally, the samples were dried in a desiccator under nitrogen. Although no systematic repeatability study was carried out on all of the 7 syntheses, several of the studied compositions had to be prepared many times for the needs of the entire study and no deviation was observed on the composition of the synthesized powders.

2.2. Analytical methods

2.2.1. Vibrational spectroscopy

The purity of the targeted AFm-NO_3 phase was assessed by vibrational spectroscopy to validate the nature of the intercalated anion and obtain local insights on the substitution of aluminum by trivalent iron cations.

- Raman spectroscopy was used to identify the intercalated anion and verify phase purity. Analyses were carried out using a T64000 Jobin Yvon spectrometer equipped with an Olympus BX41 confocal microscope at ×100 magnification.
- Infrared (IR) spectroscopy was employed to highlight Fe^{3+} to Al^{3+} substitution. Spectra were recorded in transmission mode by manually grinding the samples (2 mg) with KBr (198 mg), forming pellets. The measurements were performed using a Thermo Scientific Nicolet 5700 spectrometer in the energy range from 400 to 4000 cm^{-1}. A recording of 64 scans was performed with a resolution of 4 cm^{-1}. A background measurement was conducted using a KBr pellet before any sample analysis.

2.2.2. Mössbauer spectroscopy

Mössbauer spectroscopy was performed using a ^{57}Co source to identify and quantify the iron-containing phases, this with the primary aim of evidencing or disproving the presence of an amorphous iron hydroxide. The synthetic Fe-based AFm-NO_3 sample was transferred to a cold head cryostat under an inert He atmosphere. Spectra were recorded with a constant acceleration spectrometer with a velocity range of ±11 mm/s at room temperature, at 9 K, and at 4 K.

2.2.3. Elementary analyses

The synthetic AFm samples' elementary quantification was performed using Inductively Coupled Plasma Optical Emission Spectroscopy (ICP-OES) and Ion chromatography techniques. In both cases, the samples were diluted and acidified (0.5 % HBF_4) beforehand. The cations Ca^{2+}, Al^{3+}, and Fe^{3+}/Fe^{2+} (undifferentiated) were quantified by ICP-OES; the NO_3^- anions were quantified by chromatography.

2.2.4. X-ray powder diffraction

- X-Ray powder Diffraction (XRD) was used to determine the crystalline phase composition of the synthesized samples. The measurements were carried out using a PANalytical X'Pert-Pro diffractometer with Cu K_α radiation ($\lambda = 1.54155$ Å) equipped with an X'celerator detector in θ-θ geometry. Rietveld analyses were performed on the X-ray powder patterns using FullProf software [22]. Three crystalline phases were used for the Rietveld analyses: the nitrated AFm-NO_3 phase described with trigonal symmetry [8], the carbonated AFm-CO_3 phase described with triclinic symmetry [23], and the rhombohedral $CaCO_3$ calcite phase [24].
- High-temperature XRD (HTK), which involves recording X-ray diffractograms at different temperatures, was performed using a PANalytical X'Pert Pro diffractometer equipped with an ANTON PAAR HTK 16 heating chamber and a platinum sample holder. A heating temperature ramp of 5 °C/min was applied. HTK patterns were recorded for a temperature range from 25 °C to 275 °C; with 10 °C increments up to 150 °C, and then with 20 °C increments up to 275 °C.
- In-situ XRD analyses were conducted under controlled atmosphere to study the influence of humidity on the stability of the synthesized AFm phases using a homemade setup. An N_2 gas flow was bubbled through an ultrapure-water-filled bottle. The obtained water-saturated N_2 gas was then injected into the airtight XRD cell containing the sample to be analyzed. This cell (volume 19 mL) consisted of a cylindrical Kapton dome to avoid disturbing the XRD signal. Once the sample in place, X-ray diffractograms were recorded every 30 min for 24 h to obtain well-defined XRD patterns and capture specific changes linked to hydration levels.
- Another homemade XRD cell (Fig. 2) was designed to study the phenomena of anionic exchange in AFm phases. For this purpose, the sample was placed in a cavity at the sample holder's center, with an aqueous solution containing the anions to be exchanged surrounding this cavity. Anion transfer was achieved via blotting paper connecting the sample to the aqueous solution (1.0 M NaCl and 0.5 M Na_2CO_3). A dome was positioned above the sample holder to minimize the risk of water evaporation and contact with ambient air. X-ray diffractograms were recorded every 30 min for 48 h. More details are available on comments from Fig. SI-1.

2.2.5. Transmission electronic microscopy

TEM images were taken using a Hitachi 7650 microscope at an acceleration voltage of 200 kV. A 20 µL-droplet of the desired absolute ethanol suspension was deposited onto a copper grid (400 mesh) and left to dry at room temperature. Suspensions were prepared using 1 mg of synthetic AFm phases in 1 ml of absolute ethanol with overnight agitation.

2.2.6. Thermogravimetric analyses

TGA were performed using a Setaram SETSYS Evolution thermogravimetric analyzer 92, under an N_2 gas flow (25 mL/min), in the temperature range of 25–1000 °C with a linear temperature ramp of 5 °C/min.

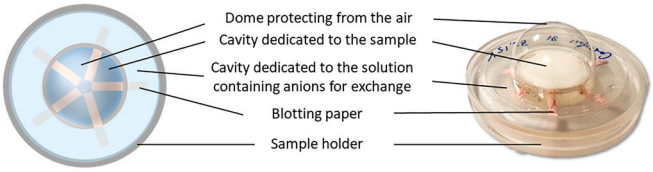

Fig. 2. Schematic representation and image of the homemade XRD cell for anionic exchange acquisitions.

3. Results and discussion

3.1. AFm-NO_3 phase characterization

3.1.1. Sample composition

The seven synthesized AFm samples were first analyzed by XRD to verify their crystalline phase composition. The obtained powder patterns (Fig. 3) unequivocally validate the precipitation of layered AFm-type compounds with diffraction peak positions corresponding to the nitrated $Ca_2Al_{1-x}Fe_x(OH)_6{\cdot}NO_3{\cdot}2H_2O$ AFm phase [17]. This phase exhibits a hexagonal lattice with trigonal $P\bar{3}c1$ symmetry. Samples from the Al-rich side display the presence of crystalline AFm-CO_3 and calcite impurities, attributable to CO_2 contamination arising from ambient air exposure during the washing process. Rietveld refinement enabled the weight fractions of the crystalline phases to be identified. Calcite was indeed observed for the $Ca_2Al_{1-x}Fe_x(OH)_6{\cdot}NO_3{\cdot}2H_2O$ samples with $0 \geq x \geq 0.5$. Although the carbonated triclinic phase $Ca_2Al_{1-x}Fe_x(OH)_6{\cdot}(CO_3)_{0.5}{\cdot}2.5H_2O$ (labeled AFm-CO_3) is clearly identified only for $0 \geq x \geq 0.67$, it was modeled for all of the samples. Indeed, an increase in the (00*l*) diffraction peak width linked to the iron substitution rate generates an unresolved overlap of scattering signals from the two AFm phases. Table 2 presents the quantitative extractions from the Rietveld analyses considering the pure nitrated $Ca_2Al_{1-x}Fe_x(OH)_6{\cdot}NO_3{\cdot}2H_2O$ phase, pure carbonated $Ca_2Al_{1-x}Fe_x(OH)_6{\cdot}(CO_3)_{0.5}{\cdot}2.5H_2O$ phase, and calcite when observed. Initially, these results seem to indicate a decreasing carbonation level of the samples with increasing iron content.

Raman and IR analyses were performed to evidence the anion intercalated into the AFm interlayer and to observe the Fe^{3+} to Al^{3+} substitution in the main layer. Symmetric stretching $\nu_1(A_1)$ vibration is the stronger Raman active mode for nitrate. This mode was observed at 1060 cm^{-1} for the aluminate $Ca_2Al(OH)_6{\cdot}NO_3{\cdot}2H_2O$ synthesis, in agreement with the literature [17]. Surprisingly, this stretching A_1 mode presents an additional contribution at 1049 cm^{-1} upon the introduction of Fe (Fig. 4), already visible for $x = 0.17$ ($Ca_2Al_{0.83}Fe_{0.17}(OH)_6{\cdot}NO_3{\cdot}2H_2O$); i.e. the weakest iron substitution tested. However, such a double ν_1 vibration for nitrate anion in the AFm structure has already been described and assigned for the Fe-based $Ca_2Fe(OH)_6{\cdot}NO_3{\cdot}2H_2O$ compound at 1044 and 1055 cm^{-1} [10]. The second ν_1 contribution has been explained by the presence of at least two distinct environments for the nitrate anion intercalated between the layers. A Raman symmetric stretching vibration related to [$Al(OH)_6$] octahedra was observed at 533 cm^{-1} for $Ca_2Al(OH)_6{\cdot}NO_3{\cdot}2H_2O$ [25], with a shift to 510 cm^{-1} observed for the [$Fe(OH)_6$] octahedra in $Ca_2Fe(OH)_6{\cdot}NO_3{\cdot}2H_2O$ [10]. The shift toward lower wavenumbers agrees with the higher ionic radius for Fe^{3+} compared to Al^{3+} ($R^{3+}_{Al} = 0.535$ Å, $R^{3+}_{Fe} = 0.645$ Å). Raman spectra of tested samples show the gradual replacement of a band centered at 533 cm^{-1} for $Ca_2Al(OH)_6{\cdot}NO_3{\cdot}2H_2O$ by one at 510 cm^{-1} for $Ca_2Fe(OH)_6{\cdot}NO_3{\cdot}2H_2O$, correlated to the gradual Fe^{3+} to Al^{3+} substitution (Fig. 4). Each of the IR spectra shown in Fig. 5 also presents one mode of the intercalated nitrate (the $\nu_2(A_2)$ bending mode) continuously present for the whole series, and Ca-O-M^{3+} bending with vibration at 787 cm^{-1} for Al^{3+} in $Ca_2Al(OH)_6{\cdot}NO_3{\cdot}2H_2O$ and at 741 cm^{-1} for Fe^{3+} in $Ca_2Fe(OH)_6{\cdot}NO_3{\cdot}2H_2O$. The IR spectra series once again characterizes the gradual Fe^{3+} to Al^{3+} substitution (Fig. 5).

Quantitative elemental analyses carried out by ICP and ion chromatography methods verify the expected atomic ratios corresponding to expected single-phase AFm-NO_3 samples (i.e. $Ca/(Al^{3+}+Fe^{3+}) = 2$, $Ca/NO_3 = 2$, $(Al^{3+}+Fe^{3+})/NO_3 = 1$ and $Fe^{3+}/(Al^{3+}+Fe^{3+}) = x$, with the x the iron substitution level in $Ca_2Al_{1-x}Fe_x(OH)_6{\cdot}NO_3{\cdot}2H_2O$). Experimental results gathered in Table 2 show $Fe^{3+}/(Al^{3+}+Fe^{3+})$ ratios close to the targeted values, $Ca/(Al^{3+}+Fe^{3+})$ ratios deviating slightly, and Ca/NO_3 and $(Al^{3+}+Fe^{3+})/NO_3$ ratios much higher than expected. The deviation from the expected $Ca/(Al^{3+}+Fe^{3+})$ ratio can be attributed to the precipitation of an amorphous impurity ($Al(OH)_3$ or $Fe(OH)_3$ for $Ca/(Al^{3+}+Fe^{3+})$ values lower than 2; or $CaCO_3$ or $Ca(OH)_2$ for $Ca/(Al^{3+}+Fe^{3+})$ values higher than 2), while the deviations from the ratios involving NO_3 evidence significant carbonation of the samples (in agreement with the presence of the AFm-CO_3 and $CaCO_3$ phases detected by XRD).

Mössbauer spectroscopy analysis was conducted on the iron present in the $Ca_2Fe(OH)_6{\cdot}NO_3{\cdot}2H_2O$ sample to assess the potential occurrence of amorphous iron-containing impurities; namely iron oxyhydroxide. The spectrum measured at room temperature (Fig. 6a) clearly shows the presence of one main doublet with slight asymmetry. This asymmetry was in fact well fitted by considering two distinct Fe^{3+} doublets (Table 3). The main component (D1 with an abundance of 87 at. %) presents an isomer shift of 0.37 mm/s (characteristic to octahedral Fe^{3+}) as already determined for the chloride $Ca_2Fe(OH)_6{\cdot}Cl{\cdot}2H_2O$ phase [26]. The second minor doublet is therefore attributed to an amorphous iron-containing impurity not detected by X-ray diffraction. The isomer shift of 0.19 mm/s is rather to be attributed to the tetrahedral environment of Fe^{3+}. Lowering the temperature to 9 K results in the same spectrum deconvolution with two quite similar paramagnetic Fe^{3+} doublets (Fig. 6b, Table 3, with changes of the Mössbauer IS and QS parameters attributed, respectively, to temperature effects on second-order Doppler shift and electric field gradient). At 4 K, the weaker contribution turned into a sextet characteristic of magnetic behavior (Fig. 6c, Table 3). These temperature observations indicate that approximately 13 atomic % of total Fe are not included in the AFm phase in this $Ca_2Fe(OH)_6{\cdot}NO_3{\cdot}2H_2O$ sample, but in an amorphous phase with Fe^{3+} tetrahedrally coordinated, undergoing a magnetic transition at very low temperature as observed for iron oxyhydroxides. This amorphous phase will simply be considered as $Fe(OH)_3$.

Finally, the morphology of the AFm crystals was observed under TEM (Fig. 7). Images taken from various AFm samples show a stack of well-defined hexagonal platelets characteristic of AFm crystals [27]. The hexagonal crystals exhibit significant size variations, from 200 nm to 1 μm (thickness cannot be estimated here).

All the experimental results presented above confirmed the precipitation of the AFm phase inserting the nitrate anions, i.e. the AFm-NO_3 phase. However, the samples were not single phase. Impurities of carbonated AFm (i.e., AFm-CO_3), calcite, and amorphous hydroxides were highlighted. The complementarity of the techniques used enabled the phase composition of tested samples' series to be calculated. Fig. SI-2 (supplementary information file) and Table 2 show the agreement between the experimental and the calculated atomic ratio values, even though some of the experimental values deviate greatly from the targeted ones. These deviations are mainly attributed to the carbonation effect (despite the precautions taken during synthesis), and to a lesser extent to the formation of iron and/or aluminum hydroxide. On average,

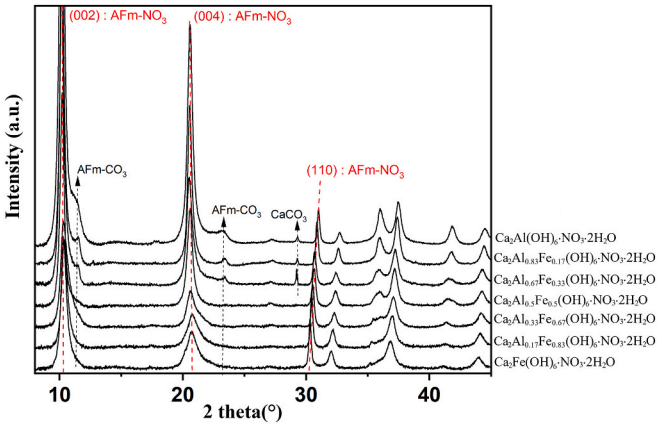

Fig. 3. XRD powder patterns of the synthesized $Ca_2Al_{1-x}Fe_x(OH)_6{\cdot}NO_3{\cdot}2H_2O$ samples showing main (002), (004), and (110) Bragg peaks from the targeted AFm-NO_3 phase, as well as AFm-CO_3 and $CaCO_3$ impurities.

Table 2
Phase composition of the synthesized samples: calculated compositions were based on experimental results (combination of the ICP/ion chromatography elementary analyses and Rietveld refinement of XRD powder patterns.

Samples	Targeted	Experimental		Calculated		
	Atomic ratios	Atomic ratios (ICP)	Phase composition (XRD + Rietveld)	Atomic ratios	Phase composition	
			weight %		weight %	mol %
$Ca_2Al(OH)_6{\cdot}NO_3{\cdot}2H_2O$	Ca/(Al + Fe) = 2 Fe/(Al + Fe) = 0 Ca/NO_3 = 2 (Al + Fe)/NO_3 = 1	Ca/(Al + Fe) = 1.81 Fe/(Al + Fe) = 0.0 Ca/NO_3 = 2.43 (Al + Fe)/NO_3 = 1.34	AFm-NO_3: 84.5 % AFm-CO_3: 14.4 % $CaCO_3$: 1.1 %	Ca/(Al + Fe) = 1.81 Fe/(Al + Fe) = 0 Ca/NO_3 = 2.43 (Al + Fe)/NO_3 = 1.34	AFm-NO_3: 81.2 % AFm-CO_3: 14.8 % $CaCO_3$: 1.0 % $Al(OH)_3$: 3.0 %	AFm-NO_3: 72.2 % AFm-CO_3: 14.2 % $CaCO_3$: 2.9 % $Al(OH)_3$:10.7 %
$Ca_2Al_{0.83}Fe_{0.17}(OH)_6{\cdot}NO_3{\cdot}2H_2O$	Ca/(Al + Fe) = 2 Fe/(Al + Fe) = 0.17 Ca/NO_3 = 2 (Al + Fe)/NO_3 = 1	Ca/(Al + Fe) = 1.99 Fe/(Al + Fe) = 0.18 Ca/NO_3 = 2.46 (Al + Fe)/NO_3 = 1.24	AFm-NO_3: 83.3 % AFm-CO_3: 15.4 % $CaCO_3$: 1.3 %	Ca/(Al + Fe) = 1.98 Fe/(Al + Fe) = 0.19 Ca/NO_3 = 2.45 (Al + Fe)/NO_3 = 1.24	AFm-NO_3: 82.7 % AFm-CO_3: 15.3 % $CaCO_3$: 1.3 % $Fe(OH)_3$: 0.7 %	AFm-NO_3: 77.8 % AFm-CO_3: 15.6 % $CaCO_3$: 3.8 % $Fe(OH)_3$: 2.9 %
$Ca_2Al_{0.67}Fe_{0.33}(OH)_6{\cdot}NO_3{\cdot}2H_2O$	Ca/(Al + Fe) = 2 Fe/(Al + Fe) = 0.33 Ca/NO_3 = 2 (Al + Fe)/NO_3 = 1	Ca/(Al + Fe) = 1.96 Fe/(Al + Fe) = 0.35 Ca/NO_3 = 2.49 (Al + Fe)/NO_3 = 1.27	AFm-NO_3: 86.7 % AFm-CO_3: 11.1 % $CaCO_3$: 2.2 %	Ca/(Al + Fe) = 1.97 Fe/(Al + Fe) = 0.36 Ca/NO_3 = 2.48 (Al + Fe)/NO_3 = 1.26	AFm-NO_3: 81.3 % AFm-CO_3: 14.9 % $CaCO_3$: 2.2 % $Fe(OH)_3$: 1.6 %	AFm-NO_3: 74.6 % AFm-CO_3: 14.8 % $CaCO_3$: 6.3 % $Fe(OH)_3$: 4.4 %
$Ca_2Al_{0.5}Fe_{0.5}(OH)_6{\cdot}NO_3{\cdot}2H_2O$	Ca/(Al + Fe) = 2 Fe/(Al + Fe) = 0.5 Ca/NO_3 = 2 (Al + Fe)/NO_3 = 1	Ca/(Al + Fe) = 2.08 Fe/(Al + Fe) = 0.52 Ca/NO_3 = 2.56 (Al + Fe)/NO_3 = 1.23	AFm-NO_3: 94.8 % AFm-CO_3: 4.4 % $CaCO_3$: 0.8 %	Ca/(Al + Fe) = 2.08 Fe/(Al + Fe) = 0.51 Ca/NO_3 = 2.56 (Al + Fe)/NO_3 = 1.23	AFm-NO_3: 80.3 % AFm-CO_3: 15.4 % $CaCO_3$: 3.6 % $Fe(OH)_3$: 0.7 %	AFm-NO_3: 72.6 % AFm-CO_3: 15.0 % $CaCO_3$: 10.7 % $Fe(OH)_3$: 1.8 %
$Ca_2Al_{0.33}Fe_{0.67}(OH)_6{\cdot}NO_3{\cdot}2H_2O$	Ca/(Al + Fe) = 2 Fe/(Al + Fe) = 0.67 Ca/NO_3 = 2 (Al + Fe)/NO_3 = 1	Ca/(Al + Fe) = 2.01 Fe/(Al + Fe) = 0.69 Ca/NO_3 = 2.82 (Al + Fe)/NO_3 = 1.40	AFm-NO_3: 93.8 % AFm-CO_3: 6.2 %	Ca/(Al + Fe) = 2.01 Fe/(Al + Fe) = 0.68 Ca/NO_3 = 2.81 (Al + Fe)/NO_3 = 1.40	AFm-NO_3: 72.5 % AFm-CO_3: 25.2 % $CaCO_3$: 1.6 % $Fe(OH)_3$: 0.7 %	AFm-NO_3: 68.0 % AFm-CO_3: 25.4 % $CaCO_3$: 4.7 % $Fe(OH)_3$: 1.9 %
$Ca_2Al_{0.17}Fe_{0.83}(OH)_6{\cdot}NO_3{\cdot}2H_2O$	Ca/(Al + Fe) = 2 Fe/(Al + Fe) = 0.83 Ca/NO_3 = 2 (Al + Fe)/NO_3 = 1	Ca/(Al + Fe) = 2.01 Fe/(Al + Fe) = 0.86 Ca/NO_3 = 2.74 (Al + Fe)/NO_3 = 1.36	AFm-NO_3: 96.1 % AFm-CO_3: 3.9 %	Ca/(Al + Fe) = 2.01 Fe/(Al + Fe) = 0.84 Ca/NO_3 = 2.74 (Al + Fe)/NO_3 = 1.36	AFm-NO_3: 74.6 % AFm-CO_3: 22.3 % $CaCO_3$: 2.1 % $Fe(OH)_3$: 1.0 %	AFm-NO_3: 68.8 % AFm-CO_3: 22.1 % $CaCO_3$: 6.4 % $Fe(OH)_3$: 2.7 %
$Ca_2Fe(OH)_6{\cdot}NO_3{\cdot}2H_2O$	Ca/(Al + Fe) = 2 Fe/(Al + Fe) = 1 Ca/NO_3 = 2 (Al + Fe)/NO_3 = 1	Ca/(Al + Fe) = 1.88 Fe/(Al + Fe) = 0.99 Ca/NO_3 = 2.58 (Al + Fe)/NO_3 = 1.37	AFm-NO_3: 93.5 % AFm-CO_3: 6.5 %	Ca/(Al + Fe) = 1.88 Fe/(Al + Fe) = 1 Ca/NO_3 = 2.59 (Al + Fe)/NO_3 = 1.38	AFm-NO_3: 76.9 % AFm-CO_3: 21.1 % $CaCO_3$: 0.0 % $Fe(OH)_3$: 2.0 %	AFm-NO_3: 72.6 % AFm-CO_3: 21.4 % $CaCO_3$: 0.0 % $Fe(OH)_3$: 6.0 %

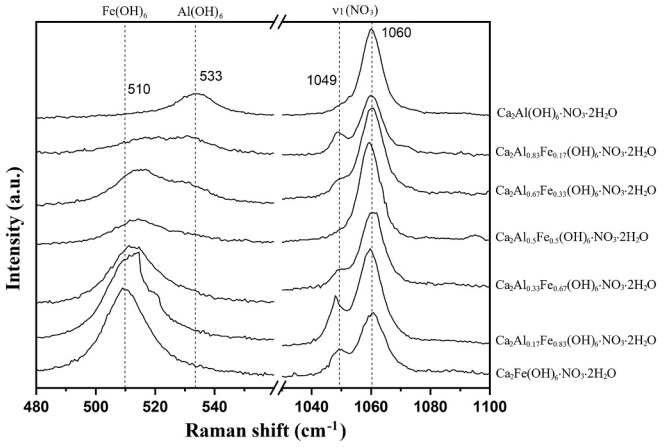

Fig. 4. Raman spectra for the $Ca_2Al_{1-x}Fe_x(OH)_6{\cdot}NO_3{\cdot}2H_2O$ series showing the nitrate ν_1 symmetric stretching mode and $[M^{3+}(OH)_6]$ octahedral stretching.

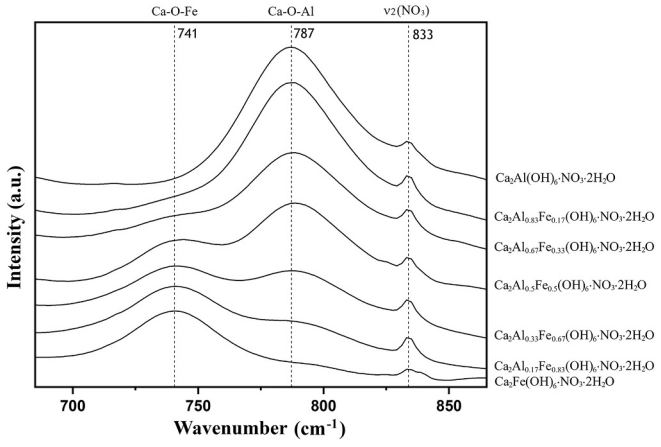

Fig. 5. IR spectra for the $Ca_2Al_{1-x}Fe_x(OH)_6{\cdot}NO_3{\cdot}2H_2O$ series showing the nitrate ν_2 bending mode and Ca-O-M^{3+}bending vibration.

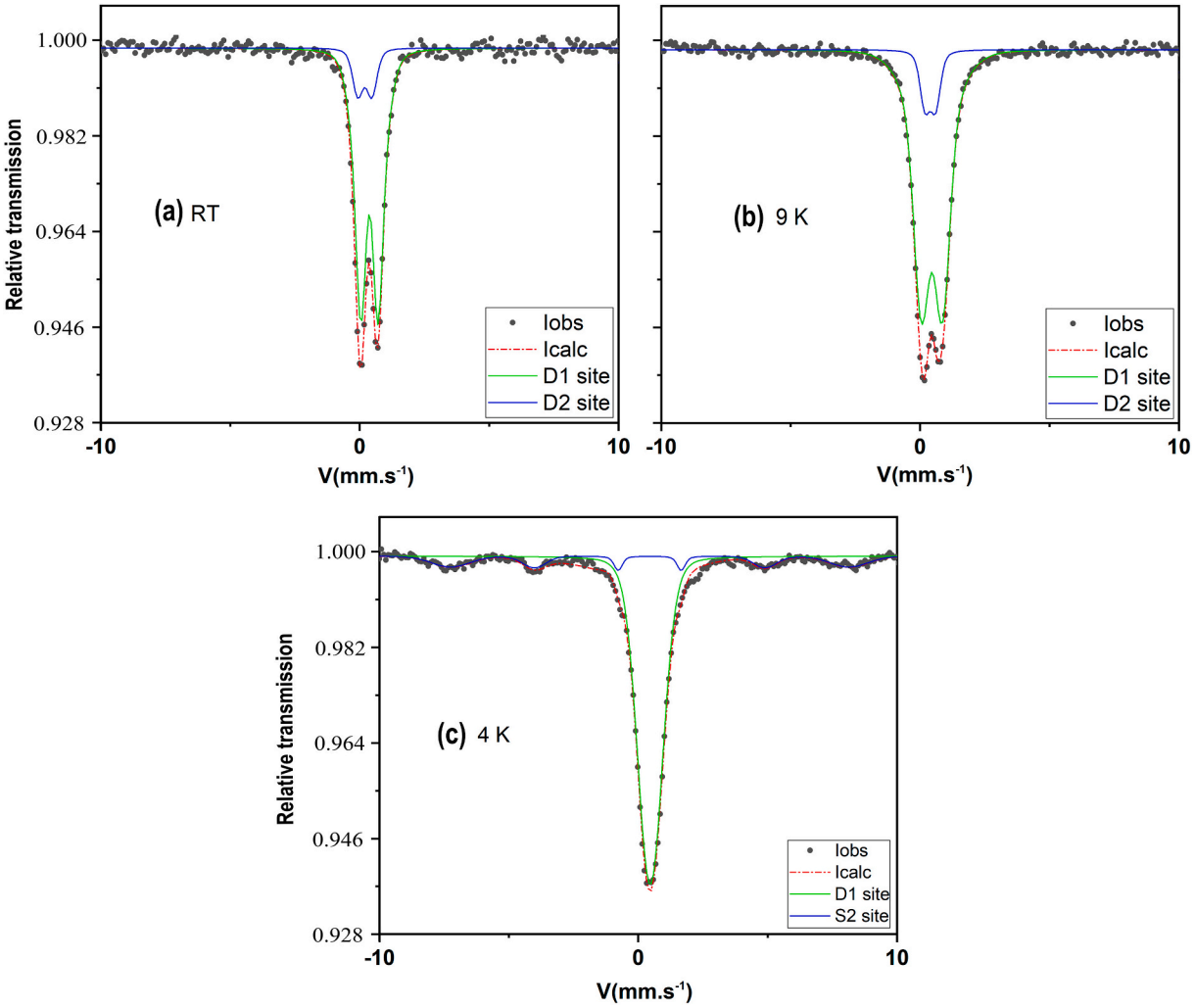

Fig. 6. Mössbauer spectra of the $Ca_2Fe(OH)_6{\cdot}NO_3{\cdot}2H_2O$ sample recorded at (a) room temperature, (b) 9 K, and (c) 4 K.

Table 3
^{57}Fe Mössbauer hyperfine parameters for the iron $Ca_2Fe(OH)_6{\cdot}NO_3{\cdot}2H_2O$ sample at different temperatures.

T (K)	Site	IS (mm/s)	QS or ε (mm/s)	H (kOe)	Population (%)
RT	D1 Fe^{3+}	0.37	0.77		87
	D2 Fe^{3+}	0.19	0.54		13
9 K	D1 Fe^{3+}	0.45	1.02		89
	D2 Fe^{3+}	0.39	0.42		11
4 K	D1 Fe^{3+}	0.45	0.71		85
	S2 sextet	0.44	0.05	477	15

the synthesized samples contain 78.5 weight % (wt%) of the AFm-NO_3 phase. The effect of carbonation generates on average 18.5 wt% AFm-CO_3 and 1.5 wt% $CaCO_3$. An average of 1.5 wt% $Al(OH)_3/Fe(OH)_3$ completes these compositions. The calculated molar % of $Fe(OH)_3$ (6.0 % - Table 2) in the iron-rich sample $Ca_2Fe(OH)_6{\cdot}NO_3{\cdot}2H_2O$ is coherent with the 13 atomic % of Fe (corresponding to 13 mol% of $Fe(OH)_3$) outside of the AFm phases, as extracted from Mössbauer spectroscopy analysis (Table 3). This Mössbauer analysis, whose precision regarding iron populations is ±5 %, provides additional confirmation of the accuracy of the calculated compositions of the synthesized samples.

An interesting point is the comparison of the weight amounts of the two AFm phases extracted from Rietveld refinement on one hand, and with calculations based on atomic ratios on the other hand (Fig. SI-3 and Table 2). The X-ray powder patterns from the Al-rich side samples evidence the presence of both AFm-NO_3 and AFm-CO_3 phases. Thus, the defined compounds $Ca_2Al_{1-x}Fe_x(OH)_6{\cdot}NO_3{\cdot}2H_2O$ and $Ca_2Al_{1-x}Fe_x(OH)_6{\cdot}(CO_3)_{0.5}{\cdot}2.5H_2O$, without anionic exchange, were considered in this work. The convergence between the calculation and the Rietveld analyses for samples from the Al-rich side justifies this choice. However, as the iron content increases, increasing divergence is observed. The diffractograms almost fail to present a resolved AFm-CO_3 diffraction signal, leading to an underestimation of the AFm-CO_3 phase. This must be interpreted by the insertion of carbonate anions into the interlayer of the AFm-NO_3 phase – i.e. carbonate to nitrate substitution leading to $Ca_2Al_{1-x}Fe_x(OH)_6{\cdot}(NO_3)_{1-y}{\cdot}(CO_3)_{y/2}{\cdot}2H_2O$ – for the samples on the Fe-rich side. We can thus consider that the AFm-NO_3 phase can be described by the composition $Ca_2Al_{1-x}Fe_x(OH)_6{\cdot}NO_3{\cdot}2H_2O$ for $0 \leq x < 0.5$, whereas it exhibits the composition $Ca_2Al_{1-x}Fe_x(OH)_6{\cdot}(NO_3)_{0.8}{\cdot}(CO_3)_{0.1}{\cdot}2H_2O$ for $0.5 \leq x \leq 1.0$.

As a final comment on phase composition, it can be noted that the x atomic ratio of trivalent cations – $Fe^{3+}/(Al^{3+}+Fe^{3+})$ in the AFm-NO_3 phase – remains very close to the targeted values whatever the synthesis.

3.1.2. *AFm-NO_3 Vegard's laws*

Full Rietveld analyses were performed for each X-ray powder pattern (the Rietveld plot of the $Ca_2Al_{0.83}Fe_{0.17}(OH)_6{\cdot}NO_3{\cdot}2H_2O$ sample is shown in Fig. SI-4). The models used for the two AFm phases were those from the pure aluminate AFm-NO_3 with trigonal $P\bar{3}c1$ symmetry [8], and AFm-CO_3 with triclinic symmetry [23]. During the refinements, the atomic parameters (position coordinates and occupancy factors)

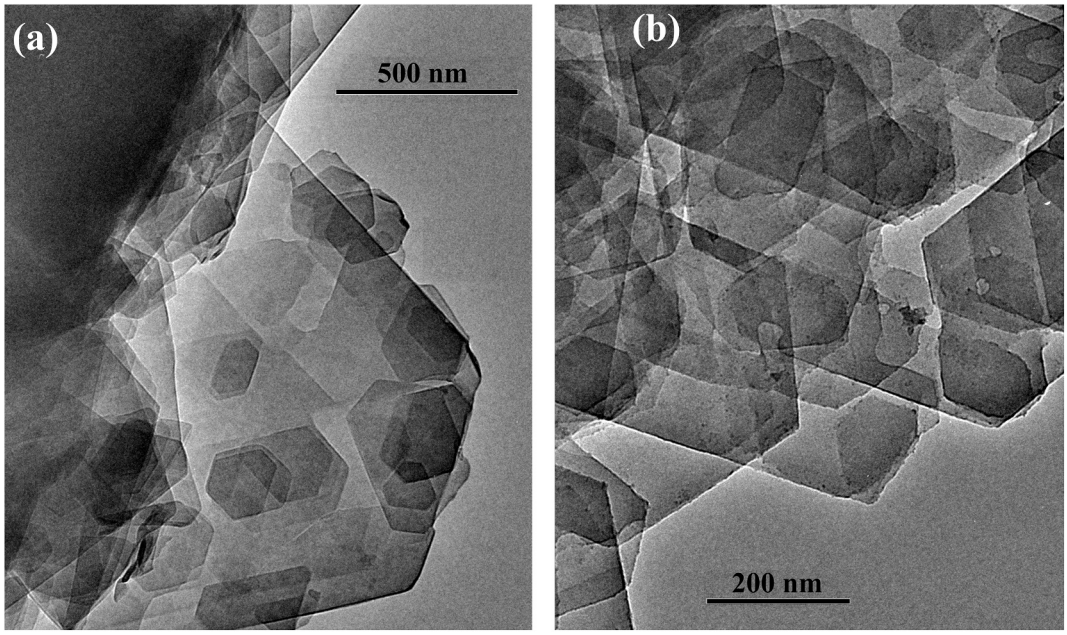

Fig. 7. TEM images from synthesized AFm crystals in samples (a) $Ca_2Al_{0.67}Fe_{0.33}(OH)_6{\cdot}NO_3{\cdot}2H_2O$ and (b) $Ca_2Al_{0.17}Fe_{0.83}(OH)_6{\cdot}NO_3{\cdot}2H_2O$.

remained fixed. Fe substitution levels were set at the targeted values. On the other hand, the lattice parameters, as well as the peak shape and thermal displacement parameters, were refined. Results obtained from Rietveld refinement are gathered in Table SI-1. X-ray powder patterns shown in Fig. 3 evidence the gradual shift of the (110) reflection toward lower angles with the introduction of iron, which is much less clear for the (00*l*) reflections. The (110) reflection, directly correlated to the lattice parameter *a*, exhibits sensitivity to the substitution of Fe^{3+} over Al^{3+}. The *a* lattice parameter of the hexagonal unit cell corresponds to the distance, in the central plane of the main layer, separating two trivalent cations. The difference between the ionic radius of Fe^{3+} (0.645 Å) and Al^{3+} (0.535 Å), in their octahedral coordination, explains the (110) shift and allows us to determine a Vegard's law representative of the *x* iron substitution level for the $Ca_2Al_{1-x}Fe_x(OH)_6{\cdot}NO_3{\cdot}2H_2O$ solid solution. The variation in cell parameter *a*, as a function of *x*, is perfectly linear (Fig. 8a), and therefore in agreement with the notion of Vegard's law. The latter can be expressed by the line equation $a = 5.766 + 0.124\,x$, which determines the iron content of the AFm-NO_3 phase thanks to its *a* lattice parameter or the position of its (110) Bragg peak. The variation in the interlayer distance (linked to the *c* hexagonal lattice parameter) is the reverse, and decreases with an increasing amount of iron (Fig. 8b). The variation is relatively linear, despite the interlayer carbonation previously determined for Fe-rich samples. The amplitude of the interlayer distance decrease is in line with the flattening of the trivalent octahedra from ~2.0 Å thickness for $Al(OH)_6$ octahedron [28] to ~1.8 Å for $Fe(OH)_6$ octahedron [29]. The linear variation of both the *a* and *c* lattice parameters for all the tested Fe/(Al + Fe) ratios tends to prove the existence of a total solid solution connecting the two 'pure' end-members.

3.2. AFm-NO_3 phase hydration levels

3.2.1. Thermal behavior

The thermal stability study of AFm phases plays a crucial role in understanding, optimizing, and predicting their properties in a wide range of industrial and environmental applications. Several hydration levels have been already reported for the pure aluminate AFm-NO_3 phase (Table 1), without any information on the impact of Fe^{3+} substitution. Thus, temperature XRD experiments were performed to identify the different AFm-NO_3 hydrates depending on iron content (experiments were conducted on the four $Ca_2Al_{1-x}Fe_x(OH)_6{\cdot}NO_3{\cdot}2H_2O$ samples with $x = 0$, 0.5, 0.67 and 1). The X-ray powder pattern series highlight that AFm-NO_3 phases behave differently depending on the Fe amount (Fig. 9).

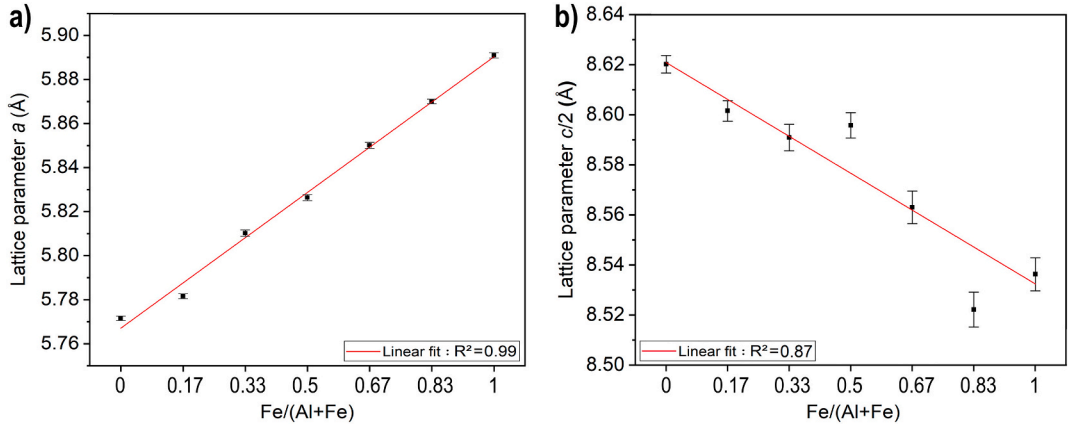

Fig. 8. Variation in lattice parameters as a function of Fe/(Al + Fe) ratio: (a) lattice parameter a and (b) d_{002} interlayer distance corresponding to c/2.

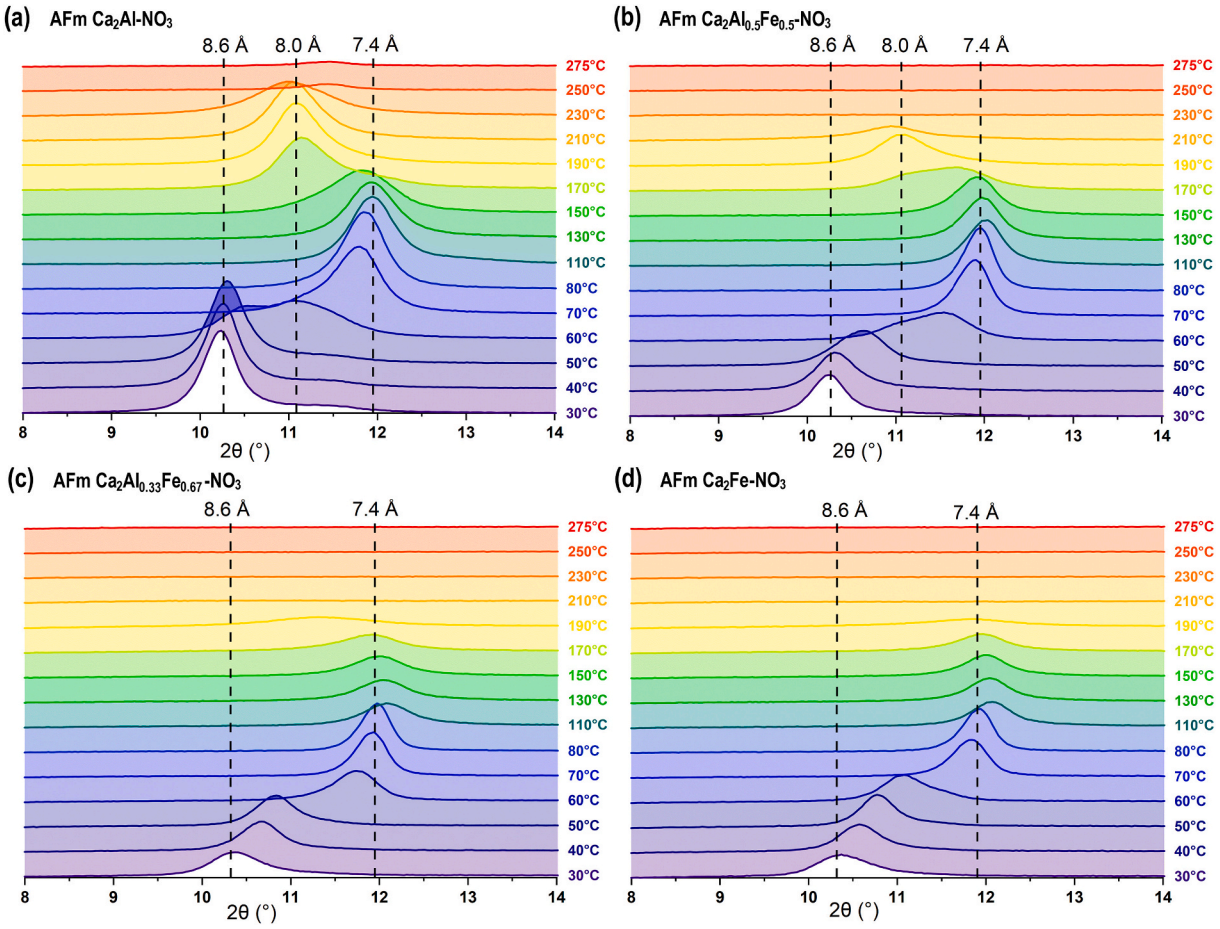

Fig. 9. Temperature-dependent X-ray powder patterns of $Ca_2Al_{1-x}Fe_x$-NO_3 samples with x = 0 (a), x = 0.5 (b), x = 0.67 (c) and x = 1 (d).

The case of the aluminate $Ca_2Al(OH)_6{\cdot}NO_3{\cdot}2H_2O$ ($x = 0$ sample, Fig. 9a) clearly evidences the existence of three hydration levels linked to three distinct interlayer distances, respectively ~8.6 Å, ~8.0 Å and ~7.4 Å. According to [8,17], the two interlayer distances of about 8.6 Å and 8.0 Å are to be attributed to $Ca_2Al(OH)_6{\cdot}NO_3{\cdot}2H_2O$ and $Ca_2Al(OH)_6{\cdot}NO_3{\cdot}1H_2O$, for which the crystal structures were solved. It should be highlighted that the $Ca_2Al(OH)_6{\cdot}NO_3{\cdot}1H_2O$ compound whose crystal structure was solved at 70 °C on a single crystal [17] was isolated here above 150 °C. However, the diffractogram recorded at 60 °C presents simultaneously these two hydrates with interlayers at 8.6 Å and 8.0 Å. On the other hand, for intermediate temperatures, a new AFm-NO_3 hydrate, with a small interlayer distance of 7.4 Å, was observed (between 70 °C and 150 °C). Such a small interlayer distance is to be related to the crystal structure of the monocarboaluminate (AFm-CO_3), whose structure was also solved on a single crystal [23]. This compound has an interlayer distance of about 7.5 Å resulting from the fact that carbonate anions are bonded to the main layer via Ca^{2+} cations and are oriented almost parallel to this main layer. This configuration is to be compared to the AFm-NO_3 structure in which nitrate anions, also bonded to Ca^{2+}, are perpendicular to the main layers. The 8.00 Å hydrate corresponds to a pillared structure with nitrate anions connecting the main layers together. This main layer connection results from Ca^{2+} bonded by two oxygen from NO_3^- [17]. Fig. 10 superimposes results extracted from X-ray powder patterns (interlayer distances) and thermogravimetric analyses considering single-phase AFm-NO_3 samples (despite the impurities characterized in Section 3.1.1). The water contents extracted from the thermograms, indicated in Fig. 10a, must therefore be taken as an indication and approximation. However, they make it possible to highlight a hydrate with two water molecules ($Ca_2Al(OH)_6{\cdot}NO_3{\cdot}2H_2O$), then a hydrate with one water molecule ($Ca_2Al(OH)_6{\cdot}NO_3{\cdot}1H_2O$), and finally the anhydrous AFm ($Ca_2Al(OH)_6{\cdot}NO_3$). Fig. 10a enables us to attribute the 8.6 Å hydrate to the composition $Ca_2Al(OH)_6{\cdot}NO_3{\cdot}{\sim}2H_2O$, the 7.4 Å hydrate to the composition $Ca_2Al(OH)_6{\cdot}NO_3{\cdot}{\sim}1H_2O$, and the 8.0 Å hydrate to the composition $Ca_2Al(OH)_6{\cdot}NO_3{\cdot}{\sim}0H_2O$ (an almost anhydrous compound above 150 °C). Finally, as the temperature exceeds 250 °C, the Al-pure AFm-NO_3 phase becomes amorphous, and starts to exhibit dehydroxylation (see thermogram in Fig. 10a).

The Fe-containing AFm phases exhibited similar and dissimilar thermal features. The similarity concerns the first transition from the 8.6 Å hydrate to the 7.4 Å hydrate, whereas the dissimilarity concerns the gradual disappearance of the 8.0 Å hydrate with the increase in Fe content. For the four analyzed samples (Fig. 9), the transition from the 8.6 Å hydrate to the 7.4 Å hydrate systematically appeared around 60 °C. The intermediate 7.4 Å hydrate remained stable up to the same temperature of about 170 °C for each of the four samples. The thermal behavior above this temperature of 170 °C then varied according to Fe content. The third 8.0 Å hydrate observed up to 230 °C for the aluminate $Ca_2Al(OH)_6{\cdot}NO_3{\cdot}2H_2O$ sample still existed in sample $Ca_2Al_{0.5}Fe_{0.5}(OH)_6{\cdot}NO_3{\cdot}2H_2O$ ($x = 0.5$, Fig. 9b), but only up to a temperature of 210 °C. Concerning the last two samples $Ca_2Al_{0.33}Fe_{0.67}(OH)_6{\cdot}NO_3{\cdot}2H_2O$ ($x = 0.67$, Fig. 9c) and $Ca_2Fe(OH)_6{\cdot}NO_3{\cdot}2H_2O$ ($x = 1.0$, Fig. 9d), the 8.0 Å hydrate was not observed (just barely, very little crystalized, and only at 190 °C for the $x = 0.67$ sample; Fig. 9c) and the amorphization temperature continued to decrease to 190 °C (directly from the 7.4 Å hydrate). Thus, for the iron-rich samples ($0.67 \leq x \leq 1.0$), we observe that the 7.4 Å hydrate corresponds not only to the composition with one water molecule ($Ca_2Al_{1-x}Fe_x(OH)_6{\cdot}NO_3{\cdot}1H_2O$, as observed for the Al-rich side) but extends to the anhydrous Ca_2Al_{1-}

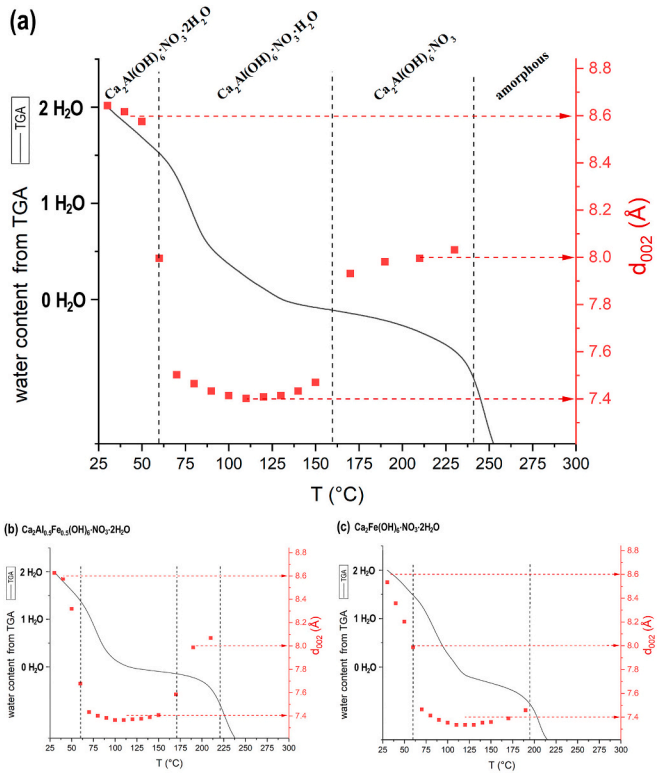

Fig. 10. Superimposition of the number of water molecules (extracted from TGA) and the AFm interlayer distance as a function of temperature for $Ca_2Al_{1-x}Fe_x$-NO_3 samples with x = 0 (a), x = 0.5 (b) and x = 1 (c).

$_xFe_x(OH)_6{\cdot}NO_3$ composition (Fig. 10c); this is contrary to the Al-rich side where the anhydrous AFm-NO_3 composition was attributed to the 8.0 Å interlayer distance, and also contrary to previous results from the literature (demonstration of an 8.0 Å hydrate for the Fe-based AFm-NO_3 compound [19]).

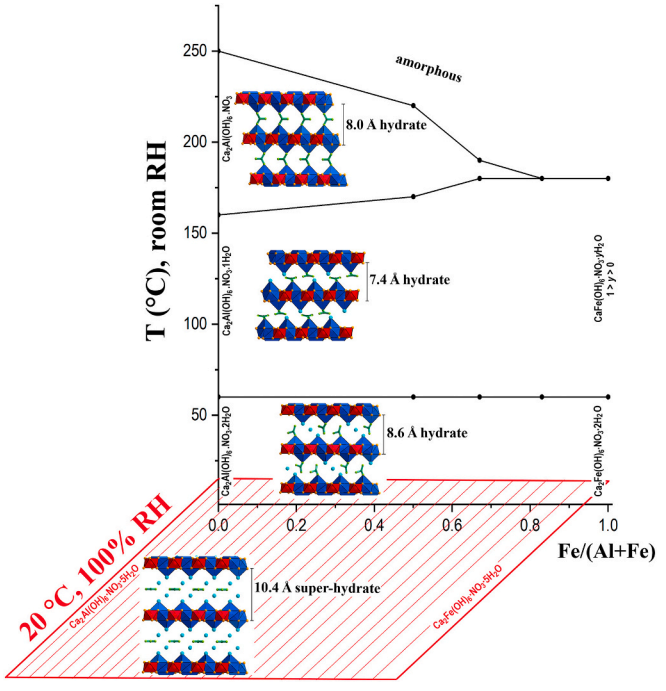

Fig. 11. Schematic stability diagram of the different hydration levels highlighted in the present work with crystal structure representations for the AFm-NO_3 system.

The thermal stability results described above enable a stability diagram (Fig. 11) to be drawn, with the different hydration levels in the investigated AFm-NO_3 system as a function of temperature and iron content. The 8.6 Å and 8.0 Å hydrate crystal diagrams represent the solved crystal structures [8,17], whereas the 7.4 Å hydrate crystal representation was produced by considering its analogy with the solved crystal structure of monocarboaluminate which presents an equivalent short interlayer distance of about 7.5 Å. This stability diagram presents a departure from the literature: the direct transition, at 60 °C, from the 8.6 Å hydrate to the 7.4 Å hydrate. However, previous studies have reported the 8.0 Å hydrate formation at 70 °C for both Al-based [17] and Fe-based [19] AFm-NO_3. A more detailed observation of the phase transition between 50 °C and 70 °C (Fig. 9 and Fig. 10) shows in fact a transient state corresponding well to an interlayer distance of 8.0 Å, indeed indicating the furtive formation of the 8.0 Å hydrate at the temperature of 60 °C. This transient state at 60 °C was visible in the Fe-based sample (Fig. 10c), for which the pillared 8.0 Å hydrate did not form at higher temperatures.

3.2.2. Humidity behavior

For both end-members of the studied AFm-NO_3 system, the literature indicates the existence of a supplementary hydrate, observed either in the wet sample or in 100 % RH condition, showing a large interlayer distance of about 10.5 Å for the Al-based compound [9] and 10.3 Å for the Fe-based compound [14,19], see Table 1. Some of the AFm samples, synthesized according to the methodology described in Section 2.1, were analyzed by in-situ X-ray diffraction in a 100 % RH airtight cell. The synthesized, then ethanol-dried, powder was placed into the dedicated cell, which was mounted onto the diffractometer. The first powder pattern acquisition was launched simultaneously with humid gas flushing (water-saturated N_2 corresponding to 100 % RH). Acquisition of the diffractograms was cycled every 30 min for one full day (Fig. 12).

The diffraction peaks associated with the AFm-CO_3 phases are attributed to impurities (from carbonation), as detailed in Section 3.1. The main diffraction peak observed in the first diffractogram in Fig. 12a corresponds to the Al-based AFm-NO_3 phase described by [8], featuring an interlayer distance of 8.61 Å, indicative of the composition $Ca_2Al(OH)_6{\cdot}NO_3{\cdot}2H_2O$ (i.e. the previously denoted 8.6 Å hydrate at 2θ = 10.3°, as expected). After only 30 min under high humidity (the second recorded diffractogram), the Al-based AFm-NO_3 phase initiated its hydration process. Indeed, a peak corresponding to an interlayer distance of 10.45 Å (2θ close to 8.5°) appeared concomitantly with the decrease in intensity of the main diffraction peak from about 10.3° 2θ. This large interlayer distance corresponds to the Al-based AFm-NO_3 hydrate isolated by [9] for which the following composition was proposed: $Ca_2Al(OH)_6{\cdot}NO_3{\cdot}5H_2O$ (called the 10.4 Å super-hydrate hereafter, see Fig. 11). We can note that this hydration process, which was rapid at first, was not complete after a day in 100 % RH. In fact, the diffractogram obtained after 3 h was not significantly different from the one obtained after 22 h (a non-negligible part of the 8.6 Å hydrate had not been converted into the 10.4 Å super-hydrate). A similar hydration mechanism was observed for the Fe-based AFm-NO_3 sample; Fig. 12b. The existence of a Fe-based super-hydrate has already been mentioned by [18] with an interlayer distance of 10.33 Å (Table 1). In the case of the present work's Fe-based sample, the 10.4 Å super-hydrate formation began more slowly but continued until the complete disappearance of the initial 8.6 Å hydrate in less than a day. However, it is difficult to estimate whether the difference in kinetics is intrinsic to the sample's composition, or due to an artefact (i.e. manner of placing the powder in the sample holder).

Two facts, observed but not shown here (Raman and XRD experiments), should be clarified about this super-hydrate (valid for both the Al- and Fe-based samples): 1/the same super-hydrate was observed on wet pastes (as observed in the following; Section 3.3), 2/this hydration process was perfectly reversible. This implies that the hydrate formed in

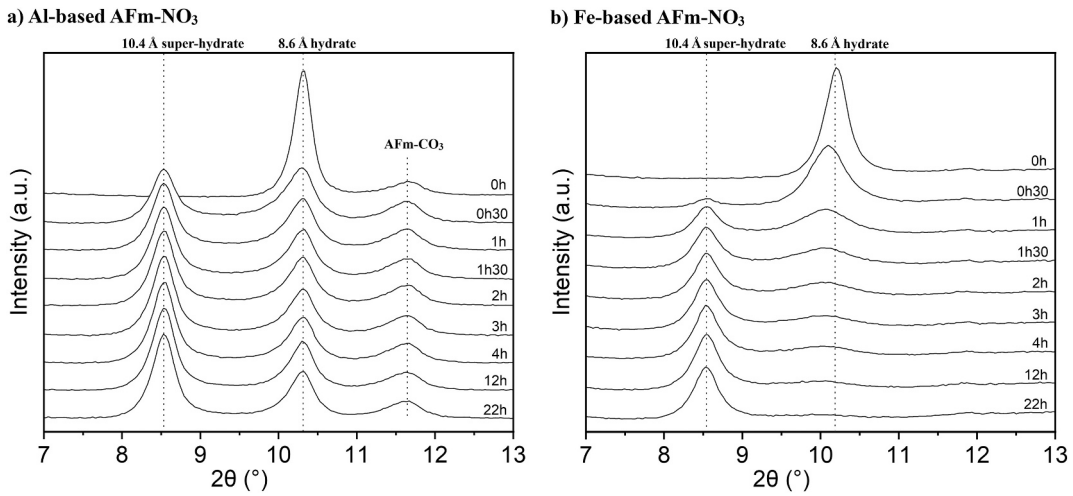

Fig. 12. In-situ X-ray diffractogram acquisition in a 100 % RH atmosphere for (a) Al-based AFm-NO_3 and (b) Fe-based AFm-NO_3 samples (AFm-CO_3 is due to synthesis carbonation).

mortar undergoing hydration is the 10.4 Å super-hydrate. Then, as the relative humidity within the porous network gradually decreased, the super-hydrate transformed into the 8.6 Å hydrate. In the same way, each time the porous network fills with water, the reversible hydration process must be considered (a phenomenon similar to swelling clays). Thus, the AFm-NO_3 phase actually precipitated in the reactor during the AFm syntheses is the 10.4 Å super-hydrate, which is destabilized in favor of the 8.6 Å hydrate due to the ethanol drying.

This super-hydrate notion is already well known for the sulfated AFm phase: the monosulfoaluminate $Ca_2Al(OH)_6{\cdot}(SO_4)_{0.5}{\cdot}3H_2O$ compound with an interlayer distance of 8.9 Å in dry concrete that transforms into the $Ca_2Al(OH)_6{\cdot}(SO_4)_{0.5}{\cdot}6H_2O$ super-hydrate in wet paste or at 100 % RH, characterized by a large interlayer distance of 10.3 Å [30]. Similar behavior exists for the $Ca_2Al(OH)_6{\cdot}OH{\cdot}3H_2O$ hydroxide-AFm and its $Ca_2Al(OH)_6{\cdot}OH{\cdot}6H_2O$ super-hydrate accompanied by an interlayer distance increase from 8.0 to 10.7 Å [30]. By analogy with the solved type II green rust crystal structure [31] – an LDH compound that presents an interlayer of the order of 10.5 Å – the crystal structure of the super-hydrate is represented in Fig. 11 with a double layer of water molecules within the interlayer region.

3.3. AFm-NO_3 phase anion exchange

Although the synthesis of the AFm-NO_3 phase is spontaneous in the presence of nitrate anions, many other anions have a greater affinity for the interlayer region of the AFm phase. This is particularly the case for carbonate (as shown by the presence of small amounts of AFm-CO_3 impurities in our samples) and chloride anions [32]. The ion exchange reactions with these two anions are interesting to follow in order to simulate the aging of a hydraulic binder containing AFm-NO_3 phase, either resulting from atmospheric carbonation or from contact with seawater. For this purpose, three samples (the two Al- and Fe-based AFm-NO_3 end-members together with the mixed $Al_{0.5}Fe_{0.5}$-AFm composition) were prepared without the final ethanol washing step, in order to promote the mobility, and then exchange, of anions in their solvated state in the wet paste. A homemade in-situ X-ray diffraction sample holder dedicated to the anion exchange study is described in Section 2.2 (analytical methods). A diffractogram was recorded every 30 min for a maximum of 2 days.

3.3.1. NO_3^- → Cl^- exchange

The X-ray diffraction patterns of the NO_3^- → Cl^- anion exchange for the two end members are presented in Fig. 13. Starting powders exhibit a diffraction signal characteristic of the AFm-NO_3 10.4 Å super-hydrate, as indicated previously (Section 3.2.2) for wet pastes. The Al-based AFm-NO_3 sample (Fig. 13a) also presents a small amount of the AFm-CO_3 impurity, with its 7.6 Å interlayer distance ($2\theta \sim 11.6°$) characteristic of monocarboaluminate $Ca_2Al(OH)_6{\cdot}(CO_3)_{0.5}{\cdot}2.5H_2O$ [23]. The

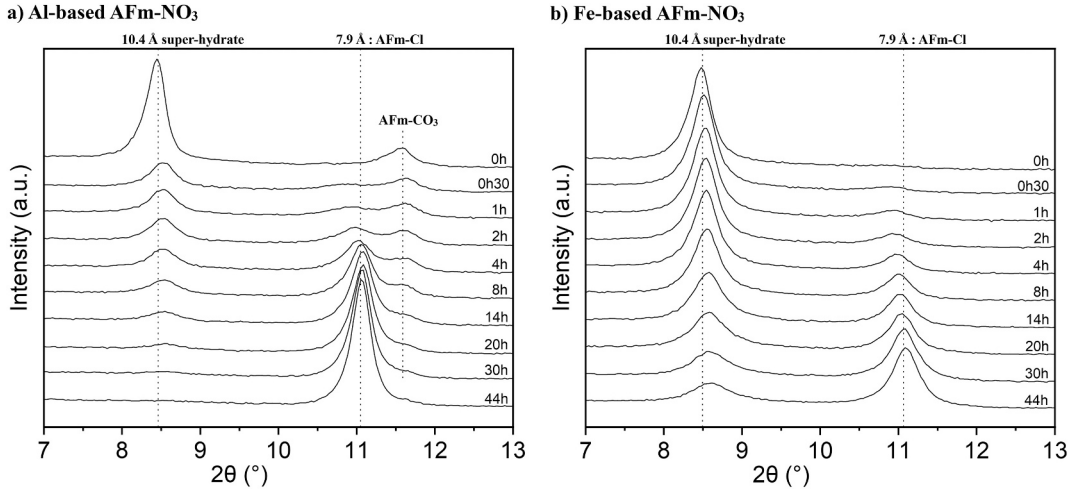

Fig. 13. Selected in-situ X-ray powder patterns during NO_3^- → Cl^- anion exchange for (a) Al-based AFm-NO_3 and (b) Fe-based AFm-NO_3 samples.

Al-based AFm-NO_3 super-hydrate diffraction signal rapidly decreases (already clearly visible in the second powder pattern) in favor of a new layered material (proved by new (00*l*) harmonics) with an interlayer distance of 7.9 Å, in agreement with the formation of the expected AFm-Cl phase: $Ca_2Al(OH)_6{\cdot}Cl{\cdot}2H_2O$ [21]. The diffraction signal of this new AFm-Cl phase becomes clear after 2 h and can be considered complete after 1 day. After 2 days' recording, the AFm-Cl phase was still stable and the only crystalline compound visible in the powder pattern.

The X-ray diffractograms of the NO_3^- to Cl^- anionic exchange for the Fe-based AFm sample are provided in Fig. 13b. Just as in the case of its Al-based analog, NO_3^- to Cl^- substitution started in the first minutes, evinced by a new weak diffraction signal close to 11.0°. As time elapsed, this characteristic $Ca_2Fe(OH)_6{\cdot}Cl{\cdot}2H_2O$ diffraction signal became more and more clear [29]. Nevertheless, the reaction was not complete after 2 days, with part of the sample still corresponding to the 10.4 Å super-hydrate form of AFm-NO_3, although NO_3^- to Cl^- substitution continued. Hence, it is noticeable that the exchange kinetics appear to be slower for the Fe-based AFm phase than for the Al-based AFm phase. In order to ensure that it was indeed a kinetic effect (and not a sample mounting artefact), the third mixed $Al_{0.5}Fe_{0.5}$-AFm sample was tested. Fig. 14a shows the same progressive transition from the 10.4 Å AFm-NO_3 super-hydrate to the chloride $Ca_2Al_{0.5}Fe_{0.5}(OH)_6{\cdot}Cl{\cdot}2H_2O$ phase also characterized by a 7.9 Å interlayer distance (similarly to the Al- and Fe-analogs). For this mixed $Ca_2Al_{0.5}Fe_{0.5}(OH)_6{\cdot}NO_3{\cdot}2H_2O$ sample, NO_3^- to Cl^- substitution also started during the first minutes of exchange and was almost complete after 20 h, similarly to the Al-based sample. Thus, it seems that exchange kinetics remain similar, but decreased, for high iron contents.

3.3.2. NO_3^- → CO_3^{2-} exchange

X-ray diffraction patterns for NO_3^- → CO_3^{2-} anionic exchange in the Al- and Fe-based AFm-NO_3 samples are presented in Fig. 15. In the initial phase, as indicated above, the 10.4 Å AFm-NO_3 super-hydrate was observed, and an AFm-CO_3 impurity was detected for the Al-based initial sample (Fig. 15a). Again, it was evidenced that AFm-NO_3 super-hydrate gradually diminished in favor of a new layered compound belonging to the AFm family. In the case of the Al-based series, the newly formed AFm phase presented an interlayer distance of 7.6 Å, whereas it was 8.0 Å for the Fe-based series. These two interlayer distances have to be linked with AFm-CO_3 phases, since the triclinic monocarboaluminate $Ca_2Al(OH)_6{\cdot}(CO_3)_{0.5}{\cdot}2.5H_2O$ phase presents an interlayer of 7.6 Å [23] and the trigonal monocarboferrate $Ca_2Fe(OH)_6{\cdot}(CO_3)_{0.5}{\cdot}2.5H_2O$ phase presents an interlayer of 8.0 Å [33]. The NO_3^- to CO_3^{2-} anion exchanges took place gradually over the 2 days of acquisition, with an almost equivalent kinetic for the AFm-NO_3 disappearance (complete after 14 h of exchange). However, the formation of the crystalline AFm-CO_3 phase was faster in the case of the Al-based sample (already at 30 min against 4 h for the Fe-based sample). On the other hand, the sequence of powder patterns for the Al-based sample evidence AFm-CO_3 destabilization in favor of $CaCO_3$ (Fig. 15a). Such AFm-CO_3 destabilization was not observed with the Fe-based sample; on the contrary, the AFm-type phases remained perfectly defined, as indicated by the unvarying (110) diffraction peak during the 2 days of the process (Fig. 15b). It therefore seems that the carbonation effect is dependent on the iron level in the AFm phase, with the stabilization of the carbonated AFm-CO_3 phase in the presence of iron.

Again, the third mixed $Al_{0.5}Fe_{0.5}$-AFm sample was used to verify the dependence on iron of AFm-CO_3 stability (Fig. 14b). Two facts were highlighted from this last exchange experiment. Firstly, the increasing stability of the AFm-CO_3 phase with respect to carbonation appears to be linked to an increasing iron content. For this $Al_{0.5}Fe_{0.5}$-AFm sample, the formation of calcite was also evidenced, but only after 20 h of acquisition (against 2 h for the Al-based sample and not observed for the Fe-based experiment). Secondly, the CO_3^{2-} to NO_3^- substitution in the mixed $Al_{0.5}Fe_{0.5}$-AFm sample occurred with the appearance of two (00*l*) harmonic series for the AFm-CO_3 phase; one linked to an interlayer distance of 8.0 Å and one linked to an interlayer distance of 7.6 Å (i.e. respectively the monocarboferrate and the monocarboaluminate). In contrast to the kinetic observations made on the Al- and Fe-pure samples from Fig. 15, the 8.0 Å AFm-CO_3 polymorph appeared first, then the 7.6 Å AFm-CO_3 polymorph was formed, and finally, these two polymorphs were destabilized in favor of $CaCO_3$ after 2 days of exchange (as already observed by [34]). Consequently, it does not seem simple to draw conclusions from our exchange experiments linking AFm-CO_3 phase stability to iron content, certainly due to artefacts from the experimental setup. Finally, it is important to mention that the anion exchange conditions used (namely the carbonate anion concentration) were very aggressive with respect to the initial AFm-NO_3 phase in order to be able to characterize the exchange kinetics in <2 days. It is thus very difficult to project this AFm-CO_3 destabilization in favor of $CaCO_3$ with regard to atmospheric carbonation in concrete or mortars based on AFm-containing bonds.

4. Conclusions

The results presented in the present work provide an exhaustive vision of the AFm-NO_3 system, whether in terms of trivalent cationic substitution, anionic exchange, or water content. The chemical behaviors elucidated thanks to the prepared synthetic samples must be transposed to the scale of cementitious materials, in particular new

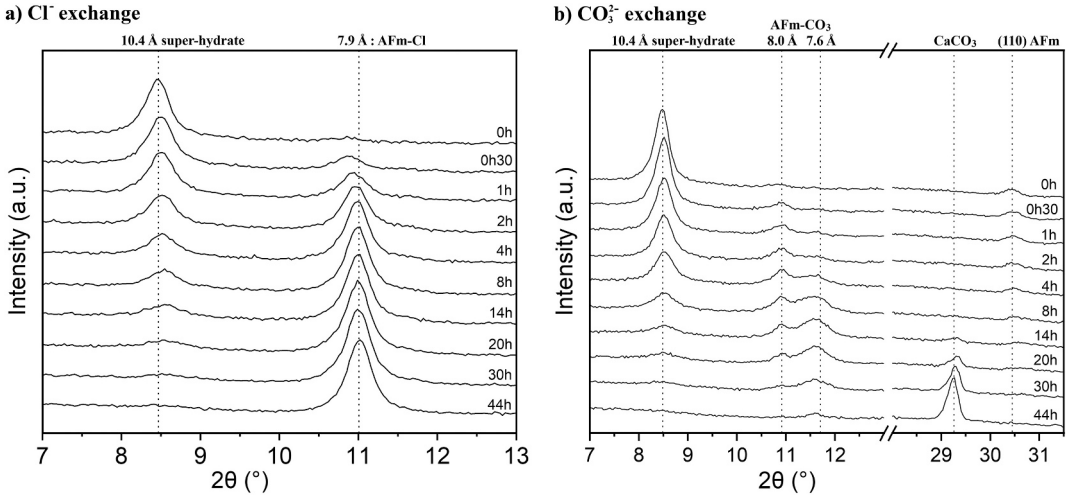

Fig. 14. Selected in-situ X-ray powder patterns during (a) NO_3^- → Cl^- anion exchange and (b) NO_3^- → CO_3^{2-} anion exchange for the mixed $Al_{0.5}Fe_{0.5}$-AFm sample.

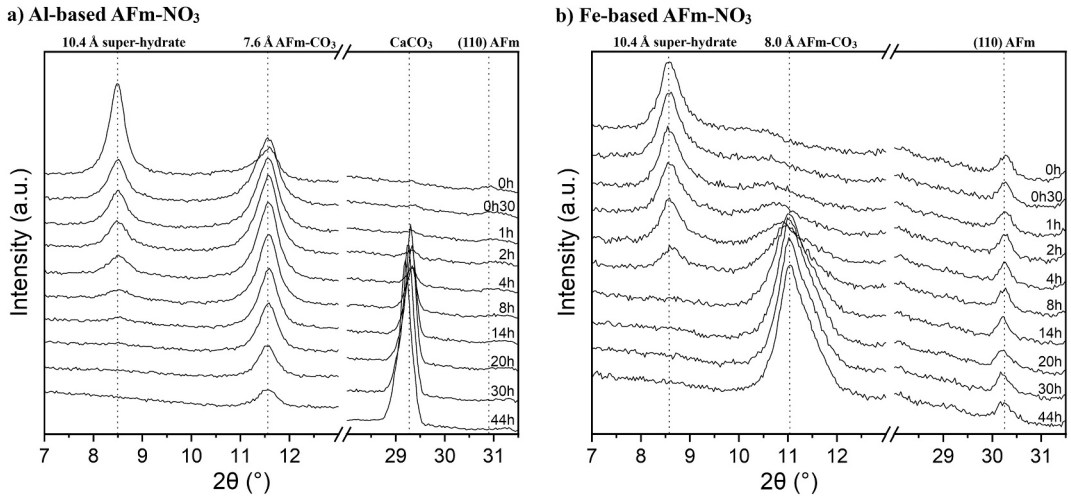

Fig. 15. Selected in-situ X-ray powder patterns during NO_3^- → CO_3^{2-} anion exchange for (a) Al-based AFm-NO_3 and (b) Fe-based AFm-NO_3 samples.

hydraulic binders containing mixed aluminum and iron oxides (and keeping in mind the potential use of nitrate anions as a setting accelerator). The work presented provides several key points:

- Composition and Structure: The synthesis and characterization of seven AFm-NO_3 samples with varying Fe/(Al + Fe) ratios were undertaken. The results elucidated the effects of compositional changes on the lattice parameters, interlayer distances, and anionic composition within the NO_3-AFm crystal structure. Structural analyses revealed the formation of a complete solid solution between the Al and Fe end-members, indicating the feasibility of substituting Al^{3+} with Fe^{3+} in the main layers. It is thus possible to use the established Vegard law based on the *a* lattice parameter (Section 3.1.2) to determine the level of Fe present in an AFm-NO_3 phase (i.e. the *x* value in $Ca_2Al_{1-x}Fe_x(OH)_6{\cdot}NO_3{\cdot}2H_2O$) precipitated in a real concrete. The study of the composition of the synthesized phases (Section 3.1.1) also showed that the Al-rich AFm-NO_3 phases have a relatively pure nitrate interlayer region ($Ca_2Al_{1-x}Fe_x(OH)_6{\cdot}NO_3{\cdot}2H_2O$ for $x < 0.5$: absence of carbonate anions). On the other hand, the Fe-rich AFm-NO_3 phases accept a non-negligible substitution of nitrate anions by carbonate ($Ca_2Al_{1-x}Fe_x(OH)_6{\cdot}(NO_3)_{0.8}(CO_3)_{0.1}{\cdot}2H_2O$ for $x \geq 0.5$).
- Hydration levels: The AFm-NO_3 encountered in ambient conditions are bi-hydrated ($Ca_2Al_{1-x}Fe_x(OH)_6{\cdot}NO_3{\cdot}2H_2O$). However, higher and lower hydration levels exist according to environmental conditions. Under high relative humidity, as well as in wet paste, the $Ca_2Al_{1-x}Fe_x(OH)_6{\cdot}NO_3{\cdot}5H_2O$ super-hydrate is formed, with the interlayer distance swelling by 20.9 % (Section 3.2.2). On the other hand, with a moderated temperature increase (about 60 °C), the lower $Ca_2Al_{1-x}Fe_x(OH)_6{\cdot}NO_3{\cdot}1H_2O$ mono-hydrate is formed with an interlayer distance shrinkage of 14.0 %. This first water molecule loss is then followed at a higher temperature (about 175 °C) by the departure of the last water molecule to reach the anhydrous $Ca_2Al_{1-x}Fe_x(OH)_6{\cdot}NO_3$ composition (Section 3.2.1). These different water amounts, correlated with changes in the interlayer distance, make AFm-NO_3 a swelling compound. The transition from the '$\cdot 5H_2O$' super-hydrate in wet paste to the '$\cdot 2H_2O$' hydrate in a dry system (with a shrinkage of 17.3 %) can be representative of the setting step of a building material based on an AFm-forming binding system. This transition is not expected to be harmful in terms of mechanical properties. On the other hand, subsequent to material hardening, the risk of AFm-NO_3 swelling (if in contact with water) must be taken into consideration in order to avoid internal stresses that could lead to physical damage (cracking), which would be problematic in terms of material durability.
- Anion Exchange Properties: Anion exchange reactions were studied to explore the ability of the AFm-NO_3 phase to capture and release environmental anions. The results demonstrated the easy exchange of nitrate (NO_3^-) with carbonate (CO_3^{2-}) or chloride (Cl^-) anions to form respectively the $Ca_2Al_{1-x}Fe_x(OH)_6{\cdot}(CO_3)_{0.5}{\cdot}2.5H_2O$ monocarbonate phase (Section 3.3.2) or $Ca_2Al_{1-x}Fe_x(OH)_6{\cdot}Cl{\cdot}2H_2O$ Friedel's related salt (Section 3.3.1). These results indicate a positive behavior of the investigated AFm-NO_3 compound in the case of carbonate (atmospheric carbonation), or chloride ingress (in a seawater environment); which can be positive in terms of corrosion resistance for reinforced concretes [35].

Overall, this study contributes to the understanding of AFm phase behavior under various conditions, which is essential in order to enhance the understanding of the hydration mechanisms of new hydraulic binders containing iron and aluminum. This research highlights the importance of considering compositional factors, thermal stability, hydration behavior, and anion exchange properties when characterizing the hydration products of these new binders.

CRediT authorship contribution statement

Aurore Lechevallier: Writing – original draft, Investigation, Formal analysis, Data curation. **Mohend Chaouche:** Supervision. **Jérôme Soudier:** Writing – review & editing, Supervision, Project administration, Investigation, Conceptualization. **Evelyne Prat:** Supervision, Funding acquisition, Conceptualization. **Guillaume Renaudin:** Writing – review & editing, Supervision, Methodology, Investigation, Formal analysis.

Declaration of competing interest

The authors declare that they have no known competing financial interests or personal relationships that could have appeared to influence the work reported in this paper.

Data availability

The authors do not have permission to share data.

Appendix A. Supplementary data

Supplementary data to this article can be found online at https://doi.org/10.1016/j.cemconres.2024.107680.

References

[1] L. Proaño, A.T. Sarmiento, M. Figueredo, M. Cobo, Techno-economic evaluation of indirect carbonation for CO2 emissions capture in cement industry: a system dynamics approach, J. Clean. Prod. 263 (2020), https://doi.org/10.1016/j.jclepro.2020.121457.

[2] W.C. Hansen, L.T. Brownmiller, R.H. Bogue, Studies on the system calcium oxide-alumina-ferric oxide, J. Am. Chem. Soc. 50 (1928) 396–406, https://doi.org/10.1021/ja01389a023.

[3] F. Sorrentino, D. Damidot, C. Fentiman, CaO-SiO2-Al2O3-Fe Oxides Chemical System: Description and Applications, 2021, https://doi.org/10.1051/978-2-7598-2536-3.

[4] P. Hewlett, M. Liska, Lea's Chemistry of Cement and Concrete, Butterworth-Heinemann, 2019.

[5] M. Bellotto, B. Rebours, O. Clause, J. Lynch, D. Bazin, E. Elkaïm, A reexamination of hydrotalcite crystal chemistry, J. Phys. Chem. 100 (1996) 8527–8534, https://doi.org/10.1021/jp960039j.

[6] M. Sacerdoti, E. Passaglia, Hydrocalumite from Latium, Italy: its crystal structure and relationship with related synthetic phases, Hydrocalumite Latium Italy Its Cryst. Struct. Relatsh. Relat. Synth. Phases (1988) 462–475.

[7] N. Chikh, M. Cheikh-Zouaoui, S. Aggoun, R. Duval, Effects of calcium nitrate and triisopropanolamine on the setting and strength evolution of Portland cement pastes, Mater. Struct. 41 (2008) 31–36, https://doi.org/10.1617/s11527-006-9215-8.

[8] G. Renaudin, M. François, The lamellar double-hydroxide (LDH) compound with composition 3CaO.Al2O3.Ca(NO3)2.10H2O, Acta Crystallogr. Sect. C 55 (1999) 835–838, https://doi.org/10.1107/S0108270199003066.

[9] M. Balonis, M. Mędala, F.P. Glasser, Influence of calcium nitrate and nitrite on the constitution of AFm and AFt cement hydrates, Adv. Cem. Res. 23 (2011) 129–143, https://doi.org/10.1680/adcr.10.00002.

[10] M. Al-Jaberi, S. Naille, M. Dossot, C. Ruby, Interlayer interaction in Ca–Fe layered double hydroxides intercalated with nitrate and chloride species, J. Mol. Struct. 1102 (2015) 253–260, https://doi.org/10.1016/j.molstruc.2015.08.064.

[11] J. Xie, G.-H. Gwak, M. Lee, S.-M. Paek, J.-M. Oh, Synthesis and structural analysis of ternary Ca–Al–Fe layered double hydroxides with different iron contents, Crystals 11 (2021) 1296, https://doi.org/10.3390/cryst11111296.

[12] W. Feitknecht, H.W. Buser, Über den Bau der plättchenförmigen calcium-aluminiumhydroxysalze, Helv. Chim. Acta 34 (1951) 128–142.

[13] S.J. Ahmed, L.S. Dent Glasser, H.F.W. Taylor, Crystal structures and reactions of C4AH12 and derived basic salts, in: Proceedings of the fifth International Symposium on the Chemistry of Cement, Tokyo, 1968.

[14] H.-J. Kuzel, Über die Hydratstufen der Hydroxisalze 3CaO• Me2O3• CaCl2• nH2O und 3CaO• Me2O3• Ca (NO3) 2• nH2O, Neues Jahrb. Für Mineral. Monatshefte (1970) 363–374.

[15] T.I. Rozenberg, E.D. Breitman, O.I. Gracheva, Investigation of products of interaction between calcium nitrate and tricalcium aluminate, Dokl. Akad. Nauk SSSR-Dokl. Chem. (1971) 199–201.

[16] J.Q. Dumm, P.W. Brown, Phase assemblages in the system Ca(OH)2—Al2O3—Ca(NO3)2—H2O, Adv. Cem. Res. 8 (1996) 143–153, https://doi.org/10.1680/adcr.1996.8.32.143.

[17] G. Renaudin, J.-P. Rapin, B. Humbert, M. François, Thermal behaviour of the nitrated AFm phase Ca4Al2(OH)12(NO3)2 • 4H2O and structure determination of the intermediate hydrate Ca4Al2(OH)12(NO3)2 • 2H2O, Cem. Concr. Res. 30 (2000) 307–314, https://doi.org/10.1016/S0008-8846(99)00251-3.

[18] H.-J. Kuzel, Beitrag zur Kristallchemie der Calciumaluminathydrate, 1969.

[19] F. Götz-Neunhoeffer, Synthese und mineralogische Charakterisierung von Calciumferrathydraten-Speicherminerale für die Anwendung in Reststoffdeponien, 1996.

[20] F. Goetz-Neunhoeffer, H. Pöllmann, Investigations on stability and long-term behaviour of AFm phases at higher temperatures by X-ray powder diffraction methods, Mater. Sci. Forum 228–231 (1996) 615–620, https://doi.org/10.4028/www.scientific.net/MSF.228-231.615.

[21] I. Rousselot, C. Taviot-Guého, F. Leroux, P. Léone, P. Palvadeau, J.-P. Besse, Insights on the structural chemistry of hydrocalumite and hydrotalcite-like materials: investigation of the series Ca2M3+(OH)6Cl·2H2O (M3+: Al3+, Ga3+, Fe3+, and Sc3+) by X-ray powder diffraction, J. Solid State Chem. 167 (2002) 137–144, https://doi.org/10.1006/jssc.2002.9635.

[22] J. Rodríguez-Carvajal, Program Fullprof 2k, 2005.

[23] M. François, G. Renaudin, O. Evrard, A cementitious compound with composition 3CaO.Al2O3.CaCO3.11H2O, Acta Crystallogr. C 54 (1998) 1214–1217, https://doi.org/10.1107/S0108270198004223.

[24] H. Chessin, W.C. Hamilton, B. Post, Position and thermal parameters of oxygen atoms in calcite, Acta Crystallogr. 18 (1965) 689–693, https://doi.org/10.1107/S0365110X65001585.

[25] R.L. Frost, S.J. Palmer, F. Theiss, Synthesis and Raman spectroscopic characterisation of hydrotalcites based on the formula Ca6Al2(CO3)(OH)16·4H2O, J. Raman Spectrosc. 42 (2011) 1163–1167, https://doi.org/10.1002/jrs.2827.

[26] M. Sipiczki, E. Kuzmann, Z. Homonnay, J. Megyeri, I. Pálinkó, P. Sipos, The structure and stability of CaFe layered double hydroxides with various Ca:Fe ratios studied by Mössbauer spectroscopy, X-ray diffractometry and microscopic analysis, J. Mol. Struct. 1044 (2013) 116–120, https://doi.org/10.1016/j.molstruc.2012.10.060.

[27] F.G. Buttler, L.S. Dent Glasser, H.F.W. Taylor, Studies on 4CaOAl2.O3.13H2O and the related natural mineral hydrocalumite, J. Am. Ceram. Soc. 42 (1959) 121–126, https://doi.org/10.1111/j.1151-2916.1959.tb14078.x.

[28] J.-P. Rapin, G. Renaudin, E. Elkaim, M. Francois, Structural transition of Friedel's salt 3CaO·Al2O3·CaCl2·10H2O studied by synchrotron powder diffraction, Cem. Concr. Res. 32 (2002) 513–519, https://doi.org/10.1016/S0008-8846(01)00716-5.

[29] G. Renaudin, A. Mesbah, B. Zeleke Dilnesa, M. Francois, B. Lothenbach, Crystal chemistry of iron containing cementitious AFm layered hydrates, Curr. Inorg. Chem. 5 (2015) 184–193.

[30] M.H. Roberts, New calcium aluminate hydrates, J. Appl. Chem. 7 (1957) 543–546, https://doi.org/10.1002/jctb.5010071004.

[31] L. Simon, M. François, P. Refait, G. Renaudin, M. Lelaurain, J.-M.R. Génin, Structure of the Fe(II-III) layered double hydroxysulphate green rust two from Rietveld analysis, Solid State Sci. 5 (2003) 327–334, https://doi.org/10.1016/S1293-2558(02)00019-5.

[32] X.-J. Zhao, Y.-Q. Zhu, S.-M. Xu, H.-M. Liu, P. Yin, Y.-L. Feng, H. Yan, Anion exchange behavior of MIIAl layered double hydroxides: a molecular dynamics and DFT study, Phys. Chem. Chem. Phys. 22 (2020) 19758–19768, https://doi.org/10.1039/D0CP02537B.

[33] B.Z. Dilnesa, B. Lothenbach, G. Le Saout, G. Renaudin, A. Mesbah, Y. Filinchuk, A. Wichser, E. Wieland, Iron in carbonate containing AFm phases, Cem. Concr. Res. 41 (2011) 311–323, https://doi.org/10.1016/j.cemconres.2010.11.017.

[34] J.D. Phillips, L.J. Vandeperre, Anion capture with calcium, aluminium and iron containing layered double hydroxides, J. Nucl. Mater. 416 (2011) 225–229, https://doi.org/10.1016/j.jnucmat.2010.11.101.

[35] J.Y. Park, J. Lee, M. Lim, G.-M. Go, H.-B. Cho, H.-S. Lee, Y.-H. Choa, Structure-modulated CaFe-LDHs with superior simultaneous removal of deleterious anions and corrosion protection of steel rebar, RSC Adv. 11 (2021) 10951–10961, https://doi.org/10.1039/D1RA00300C.